Eleventh International Conference on Computational Fluid Dynamics (ICCFD11), Maui, HI, USA, July 11-15, 2022

ICCFD11-2022-2702

The Harmonic Linearized Navier-Stokes Equations for Transition Prediction in Three-Dimensional Flows

P. Paredes*, M. Choudhari**, M. H. Carpenter** and F. Li**
Corresponding author: pedro.paredes@nasa.gov

* National Institute of Aerospace, Hampton, VA 23666, USA.
** NASA Langley Research Center, Hampton, VA 23681, USA.

Abstract: The conventional method to predict the onset of laminar-turbulent transition in convectively unstable boundary-layer flows is based on the logarithmic amplification ratio, the so-called N-factor, of the linear instability waves. To calculate the N-factor, the flow variables are decomposed into a laminar basic state solution and the linear disturbances, which are assumed to be harmonic in time. The most commonly used linear stability analysis approaches include the locally parallel linear stability theory (LST) and the nonlocal, weakly nonparallel parabolized stability equations (PSE). However, these methods do not account for strong streamwise gradients that are encountered in several configurations of interest, such as those in the vicinity of roughness elements, steps, gaps, or corners. To compute the linear evolution of disturbances along such strongly nonparallel regions, the harmonic linearized Navier-Stokes equations (HLNSE) need to be solved. The discretization of the HLNSE for spanwise/azimuthally inhomogeneous laminar basic states yields a linear system of complex arithmetic with a leading dimension of the order of 10^7 to 10^8 even in relatively simple flows. A combined multithread and multiprocessor algorithm is implemented for the direct solution of such linear systems. Results for a supersonic boundary layer over a three-dimensional roughness patch show good agreement with experimental measurements when the evolution of the instability waves over the roughness patch is included via the HLNSE. Additionally, inflow-resolvent analysis based on the HLNSE for discrete-roughness-induced disturbances in the nose tip of a blunt cone at Mach 6 demonstrates the importance of including the disturbance amplification along the near vicinity of the roughness element and separation region.

Keywords: Boundary Layer Stability, Numerical Algorithms.

1 Introduction

Laminar-turbulent transition of boundary-layer flows can have a strong impact on the performance of flight vehicles because of its influence on the surface skin friction, as well as aerodynamic heating for high-speed configurations. Therefore, the prediction and control of the transition onset are important to develop optimized designs of flight vehicles across the speed regime. Obstacles to the accurate prediction and practical deployment of laminar flow control include manufacturing defects (e.g., two-dimensional steps and gaps, surface waviness, and three-dimensional excrescences), operational factors, or geometrical aspects, as deflected control surfaces or ramps that can lead to flow separation. The physical mechanisms underlying the effects of these factors on boundary-layer transition include destabilization of convective-type instability waves [1, 2], increased boundary-layer receptivity to freestream unsteadiness [3], the presence of streak instabilities in the wakes of three-dimensional nonuniformities [4], a possible emergence of an absolute or global instability within the recirculation region near the nonuniformity [5, 6], or some combination of the above phenomena such as simultaneous receptivity and stability modification [7].

Typically, the net effect of local surface nonuniformities, i.e., steps, gaps, or humps, has been accounted for via the correlation of the jump in the N-factor envelope with the amplitude of the nonuniformity [8, 9].

Recently, the nonparallel effects of two-dimensional surface deformations on the development of instability waves have been accounted by using unsteady direct numerical simulations (DNS) [10]. However, the various studies based on the HLNSE [7, 11, 12, 13, 14, 15, 16, 17, 18] have demonstrated the utility of the HLNSE framework as an efficient and accurate alternative to DNS to predict the linear disturbance evolution in strongly nonparallel flows. The solution of the linear system of equations arising from the high-order discretization of the HLNSE for two-dimensional flow problems has a leading dimension of the order of 10 thousand to 1 million and can be resolved with sparse direct solvers, e.g., MUMPS [19]. However, the solution of three-dimensional problems becomes prohibitively expensive for sparse direct solvers as the leading dimension becomes of the order of 10 million to 100 million even for problems of moderate complexity. In the present effort, the direct solution of the three-dimensional HLNSE is performed with a combined multi-thread and multiprocessor algorithm that allows its robust solution for three-dimensional problems. A brief overview of the numerical methodology is given below. Then, the method is applied to solve the evolution of linear Mack's first-mode disturbances in a flat plate with a sinusoidal roughness patch at the conditions of the NASA Langley Research Center Supersonic Low Disturbance Tunnel (SLDT) Mach 3.5 quiet facility [20] and to study the disturbances induced by discrete roughness elements on the nose tip of a blunt cone at zero degrees angle of attack at the conditions of the experiment conducted in the Air Force Research Laboratory Mach 6 High Reynolds Number facility [15].

2 Problem Statement

The linear stability analysis is based on the decomposition of the flow variables, $\mathbf{q}(x,y,z,t) = (\rho,u,v,w,T)^T$, into a laminar basic state, $\bar{\mathbf{q}}(x,y,z) = (\bar{\rho},\bar{u},\bar{v},\bar{w},\bar{T})^T$, and the unsteady perturbations, $\tilde{\mathbf{q}}(x,y,z,t)^T$. Here, (x,y,z) denote the streamwise direction, the wall-normal direction, and the spanwise direction, respectively, while (u,v,w) represent the corresponding velocity components. The density and temperature are denoted by ρ and T, respectively. The linear perturbations are assumed to be harmonic in time and are written as

$$\tilde{\mathbf{q}}(x,y,z,t) = \hat{\mathbf{q}}(x,y,z)\exp(-\mathrm{i}\omega t) + \text{c.c.}, \tag{1}$$

where ω is the angular disturbance frequency, and c.c. refers to the complex conjugate. The disturbance vector $\hat{\mathbf{q}}(x,y,z)$ satisfies the three-dimensional HLNSE,

$$\mathcal{L}\hat{\mathbf{q}}(x,y,z) = \hat{\mathbf{f}}, \tag{2}$$

where the linear operator $\mathcal{L}$ depends on the basic state variables, flow parameters, and on the angular frequency of the perturbation, and $\hat{\mathbf{f}}$ represents an inflow condition or forcing term.

The onset of laminar-turbulent transition is estimated via correlations involving the envelope of the logarithmic amplification ratio, i.e., the so-called N-factor, relative to the lower branch neutral location x_I where the disturbance at any given frequency first becomes unstable,

$$N = \ln\left[\phi(x)/\phi(x_I)\right], \tag{3}$$

where ϕ denotes an amplitude norm of $\hat{\mathbf{q}}$, e.g., the maximum mass-flux disturbance at a given streamwise station or the energy norm E derived in Ref. [21] and used in Refs. [22, 23] for linear stability theory,

$$E(x) = \int_z \int_y \hat{\mathbf{q}}(x,y,z)^H \mathbf{M}\hat{\mathbf{q}}(x,y,z)\,\mathrm{d}y\,\mathrm{d}z, \quad \mathbf{M} = \mathrm{diag}\left[\frac{\bar{T}}{\gamma M^2\bar{\rho}}, \bar{\rho}, \bar{\rho}, \bar{\rho}, \frac{\bar{\rho}}{\gamma(\gamma-1)M^2\bar{T}}\right], \tag{4}$$

where the superscript H denotes the conjugate transpose, and $\mathbf{M}$ is the energy weight matrix.

The structure of the matrix $\mathbf{L}$ resulting from the spatial discretization of the operator $\mathcal{L}$ of Eq. (2) depends on the form of the discrete spatial derivative operators. In the present study, the streamwise coordinate is discretized with a fourth-order centered finite-difference standard scheme, while the wall-normal and spanwise directions are discretized with twelfth-order finite-difference schemes [24]. Because of the selected streamwise discretization scheme, the operator $\mathcal{L}$ becomes a block pentadiagonal (BPD) matrix $\mathbf{L}$ and the linear system of Eq. (2) becomes a BPD system of the following form

$$
\begin{bmatrix}
C_1 & D_1 & E_1 & 0 & & & & \cdots & & & 0 \\
B_2 & C_2 & D_2 & E_2 & 0 & & & & \cdots & & 0 \\
A_3 & B_3 & C_3 & D_3 & E_3 & 0 & & & & \cdots & 0 \\
\vdots & & & & \ddots & & & & & & \vdots \\
0 & \cdots & 0 & A_i & B_i & C_i & D_i & E_i & 0 & \cdots & 0 \\
\vdots & & & & & & \ddots & & & & \vdots \\
0 & & \cdots & & & 0 & A_{n-2} & B_{n-2} & C_{n-2} & D_{n-2} & E_{n-2} \\
0 & & & \cdots & & & 0 & A_{n-1} & B_{n-1} & C_{n-1} & D_{n-1} \\
0 & & & & \cdots & & & 0 & A_n & B_n & C_n
\end{bmatrix}
\begin{bmatrix} q_1 \\ q_2 \\ q_3 \\ \vdots \\ q_i \\ \vdots \\ q_{n-2} \\ q_{n-1} \\ q_n \end{bmatrix}
=
\begin{bmatrix} f_1 \\ f_2 \\ f_3 \\ \vdots \\ f_i \\ \vdots \\ f_{n-2} \\ f_{n-1} \\ f_n \end{bmatrix},
$$

where $n \equiv n_x$, $\hat{\mathbf{q}} = (q_1^T, q_2^T, \cdots q_n^T)^T$, and $\hat{\mathbf{f}} = (f_1^T, f_2^T, \cdots f_n^T)^T$. The vectors q_i and f_i and the blocks A_i, B_i, C_i, D_i, and E_i have a leading dimension of $m = 5\, n_y\, n_z$.

The direct solution of the block-pentadiagonal linear system of equations with complex arithmetic is performed by using a combined multithread and multiprocessor algorithm based on the Thomas algorithm and the dual Schur complement method. This algorithm reduces the scaling of the solution time and memory requirements on the number of streamwise points from cubic to linear and from quadratic to linear, respectively.

The Thomas algorithm [25] is a simplified form of Gaussian elimination without pivoting, as originally applied to tridiagonal systems. An efficient implementation for BPD systems is presented in Ref. [26], where BLAS and LAPACK routines are used. Here, the sparsity of the blocks A_i, B_i, C_i, D_i, and E_i is also exploited with sparse BLAS subroutines. We use the OpenMP multithread implementation of the BLAS, sparse BLAS, and LAPACK modules available in the Intel MKL package. In the Thomas algorithm, the factorization is based on the LU decomposition and is performed with the following matrix-matrix operations

$$
\begin{aligned}
K_i &= B_i - A_i Y_{i-2}, \\
G_i &= C_i - K_i Y_{i-1} - A_i Z_{i-2}, \\
Y_i &= (G_i)^{-1}(D_i - K_i Z_{i-1}), \\
Z_i &= (G_i)^{-1} E_i,
\end{aligned}
$$

where $i = 1 : 1 : n$ and $Y_{-1} = Z_{-1} = Y_0 = Z_0 = 0$. The blocks K_i, G_i, Y_i, and Z_i are dense due to the matrix inversion operation. The solution is computed with matrix-vector operations by using the forward substitution, i.e.,

$$
r_i = (G_i)^{-1}(f_i - K_i r_{i-1} - A_i r_{i-2}),
$$

where $i = 1 : 1 : n$ and $r_{-1} = r_0 = 0$, followed by the backward substitution, i.e.,

$$
q_i = r_i - Y_i q_{i+1} - Z_i q_{i+2}
$$

where $i = n : -1 : 1$ and $q_{n+1} = q_{n+2} = 0$.

By storing the LU decomposition blocks, K_i, $(G_i)^{-1}$, Y_i, and Z_i, the forward and backward substitutions can be applied to solve the linear system with different right-hand-side (RHS) vectors. The global stability analysis and resolvent analysis methods require the solution of several linear systems of equations with different RHS vectors. For the solution of the eigenvalue solution of the HLNSE operator in the global stability analysis, the shift-and-invert Arnoldi method [27] is commonly used and requires as many linear system solutions as the selected Krylov dimension. The resolvent analysis can be formulated as an iterative algorithm to find the optimal forcing for maximum response gain [28, 29] by using the discrete adjoint that is equivalent to the Hermitian HLNSE operator. However, the solution of the Hermitian system $\mathbf{L}^H \hat{\mathbf{q}}^\dagger = \hat{\mathbf{f}}^\dagger$ can also be obtained with the same LU decomposition blocks by the modified forward substitution,

$$
r_i^\dagger = f_i^\dagger - Y_i^H r_{i-1}^\dagger - Z_i^H r_{i-2}^\dagger,
$$

where $i = 1:1:n$ and $r_{-1}^{\dagger} = r_0^{\dagger} = 0$, followed by the modified backward substitution,

$$q_i^{\dagger} = (G_i^H)^{-1}(r_i^{\dagger} - K_i^H q_{i-1}^{\dagger} - A_i^H q_{i-2}^{\dagger}).$$

The dual Schur complement [30] is a direct parallel method, based on the use of nonoverlapping subdomains with implicit treatment of the interface conditions. Each processor solves its subdomain plus an interface problem to obtain the exact solution of the subdomain with only one global communication operation. The linear system $\mathbf{L}\hat{\mathbf{q}} = \hat{\mathbf{f}}$ is reordered as follows

$$\left[\begin{array}{c|c|c|c} \mathbf{L}_{1,1} & 0 & 0 & \mathbf{L}_{1,s} \\ \hline 0 & \ddots & 0 & \vdots \\ \hline 0 & 0 & \mathbf{L}_{n_p,n_p} & \mathbf{L}_{n_p,s} \\ \hline \mathbf{L}_{s,p} & \cdots & \mathbf{L}_{s,p} & \mathbf{L}_{s,s} \end{array}\right] \left[\begin{array}{c} q_1 \\ \hline \vdots \\ \hline q_{n_p} \\ \hline q_s \end{array}\right] = \left[\begin{array}{c} f_1 \\ \hline \vdots \\ \hline f_{n_p} \\ \hline f_s \end{array}\right],$$

where n_p is the number of partitions, and the solution is obtained with the following operations

$$\begin{aligned} q_s &= \tilde{\mathbf{L}}_{s,s}^{-1} \tilde{f}_s \begin{cases} \tilde{\mathbf{L}}_{s,s} = \mathbf{L}_{s,s} - \sum_{p=1}^{n_p} \mathbf{L}_{s,p}\mathbf{L}_{p,p}^{-1}\mathbf{L}_{p,s} \\ \tilde{f}_s = f_s - \sum_{p=1}^{n_p} \mathbf{L}_{s,p}\mathbf{L}_{p,p}^{-1} f_p \end{cases} \\ q_p &= \mathbf{L}_{p,p}^{-1} f_p - \mathbf{L}_{p,s} q_s; \end{aligned}$$

where $p = 1:1:n_p$. For example, a problem with $n_x = 12$ and two partitions ($n_p = 2$) would be ordered as follows

$$\left[\begin{array}{ccccc|ccccc|cc} C_1 & D_1 & E_1 & 0 & 0 & 0 & 0 & 0 & 0 & 0 & 0 & 0 \\ B_2 & C_2 & D_2 & E_2 & 0 & 0 & 0 & 0 & 0 & 0 & 0 & 0 \\ A_3 & B_3 & C_3 & D_3 & E_3 & 0 & 0 & 0 & 0 & 0 & 0 & 0 \\ 0 & A_4 & B_4 & C_4 & D_4 & 0 & 0 & 0 & 0 & 0 & E_4 & 0 \\ 0 & 0 & A_5 & B_5 & C_5 & 0 & 0 & 0 & 0 & 0 & D_5 & E_5 \\ \hline 0 & 0 & 0 & 0 & 0 & C_8 & D_8 & E_8 & 0 & 0 & A_8 & B_8 \\ 0 & 0 & 0 & 0 & 0 & B_9 & C_9 & D_9 & E_9 & 0 & 0 & A_9 \\ 0 & 0 & 0 & 0 & 0 & A_{10} & B_{10} & C_{10} & D_{10} & E_{10} & 0 & 0 \\ 0 & 0 & 0 & 0 & 0 & 0 & A_{11} & B_{11} & C_{11} & E_{11} & 0 & 0 \\ 0 & 0 & 0 & 0 & 0 & 0 & 0 & A_{12} & B_{12} & C_{12} & 0 & 0 \\ \hline 0 & 0 & 0 & A_6 & B_6 & E_6 & D_6 & 0 & 0 & 0 & C_6 & D_6 \\ 0 & 0 & 0 & & A_7 & D_7 & E_7 & 0 & 0 & 0 & B_7 & C_7 \end{array}\right] \left[\begin{array}{c} q_1 \\ q_2 \\ q_3 \\ q_4 \\ q_5 \\ \hline q_8 \\ q_9 \\ q_{10} \\ q_{11} \\ q_{12} \\ \hline q_6 \\ q_7 \end{array}\right] = \left[\begin{array}{c} f_1 \\ f_2 \\ f_3 \\ f_4 \\ f_5 \\ \hline f_8 \\ f_9 \\ f_{10} \\ f_{11} \\ f_{12} \\ \hline f_6 \\ f_7 \end{array}\right]. \tag{5}$$

The operations to form $\tilde{\mathbf{L}}_{s,s}$ require the solution of the subdomain linear systems with a matrix RHS, $\mathbf{L}_{p,p}^{-1}\mathbf{L}_{p,s}$. As shown by the example from Eq. (5), the matrices $\mathbf{L}_{p,s}$ for the first and last partitions have non-zero block entries in the last or first two rows, respectively. This property is exploited by computing the UL decomposition of the last partition instead of the LU decomposition. By doing this, the computational cost of decomposition of the first and last subdomains becomes equivalent to each other.

3 Results

The application of the three-dimensional HLNSE for the investigation of linear disturbance amplification is presented for two high-speed boundary layer configurations. The first problem corresponds to the evolution of Mack's first-mode waves over a sinusoidal roughness patch on a flat plate at Mach 3.5 wind tunnel conditions that was numerically and experimentally studied in Refs. [31, 20]. The HLNSE are used to monitor the evolution of the incoming disturbances over the roughness patch as the strongly nonparallel effects prevent an accurate solution via the PSE. In the second problem, the disturbances induced by an array of prismatic roughness elements located on the nose tip of a blunt cone at 45° from the axis at Mach 6 wind tunnel flow conditions are studied with inflow-resolvent analysis based on the three-dimensional HLNSE [32]. The HLNSE are able to account for the evolution of the disturbances over the roughness elements and the regions of flow separation in the vicinity of the elements.

3.1 Disturbance Evolution over a Sinusoidal Roughness Patch

A combination of the PSE and HLNSE methods was used in Ref. [20] to study the linear evolution of Mack's first-mode waves over a sinusoidal roughness patch in a flat plate at the conditions of the SLDT Mach 3.5 quiet tunnel. The conditions corresponded to a freestream Mach number of $M_\infty = 3.5$, a freestream temperature of $T_\infty = 92.52$ K, and a stagnation pressure of $p_0 = 241.7$ kPa, which yield a freestream Reynolds number of $Re_\infty = 12.6 \times 10^6$ m^{-1} by using the Sutherland's viscosity law for air [33]. The adiabatic wall temperature condition was used. The roughness patch was defined by sinusoidal functions in streamwise and spanwise directions with an equivalent wavelength of 6.25 mm for both directions. The edges were modified using a Gaussian error function. The leading edge of the roughness patch is located at a distance of 28.8 mm from the leading edge of the flat plate. The maximum roughness height is 272 μm. Additional geometrical details are given in Ref. [20].

As described in Ref. [31], the two-dimensional solution over the flat plate was computed by using a second-order accurate algorithm as implemented in the finite-volume compressible Navier-Stokes flow solver VULCAN-CFD [34, 35]. The two-dimensional solution was imposed at the inflow and farfield boundary located below the bow shock for the solution of the three-dimensional, spanwise-periodic, laminar boundary-layer flow over the flat plate with the sinusoidal roughness patch computed with a high-order direct numerical simulation (DNS) solver. A detailed description of the governing equations and their numerical solution is given in Ref. [36]. The inviscid fluxes from the governing equations are computed using a seventh-order weighted essentially nonoscillatory (WENO) finite-difference scheme introduced in Ref. [37]. The viscous fluxes are discretized using a fourth-order central difference scheme and time-accurate integration is performed using a third-order low-storage Runge-Kutta scheme [38]. Additional details about the computational domain and grid are given in Ref. [20].

The stability analysis of the three-dimensional flow over the plate with the sinusoidal roughness patch was performed with plane-marching PSE to study the roughness wake instabilities and by a combination of PSE and HLNSE to study the evolution of Mack's first-mode instabilities that begin to amplify upstream of the roughness. Four families of disturbances, i.e., AA, SS, SA, and AS, were identified by their lateral boundary conditions. A single roughness spanwise wavelength was discretized and symmetric (S) or antisymmetric (A) boundary conditions were used. The evolution of the AA disturbance, i.e., antisymmetric boundary conditions in both symmetry planes, with 80 kHz is shown in Fig. 1(a). The Mack's first mode with wavelength $\lambda_z = 3.125$ mm and frequency of $f = 80$ kHz becomes unstable upstream of the roughness patch, and the PSE are used to calculate its evolution up to the roughness patch. The PSE solution is imposed as the inflow condition for the HLNSE to calculate the evolution over the roughness patch with a grid of $n_x = 701$, $n_y = 61$, and $n_z = 49$ points, which yield a linear system of 10.5M DOF. Finally, the PSE are used to calculate the evolution of the disturbance along the wake of the roughness, by using the HLNSE solution as inflow condition for the PSE. Figure 1(b) shows an improved agreement of the predicted disturbance amplification spectra with the measured power spectra at $x = 153.8$ mm when the combination of PSE and HLNSE is used to calculate the evolution of disturbances over the entire plate, instead of the roughness wake instability alone with PSE. This finding confirms the significance of disturbance growth both upstream of and above the roughness patch and the effect on the growth of instabilities in the wake. The significance of the roughness nearfield on the disturbance amplification was also highlighted in the previous DNS involving roughness patches of different lenghts [31].

3.2 Distributed-Roughness-Induced Disturbances in a Blunt Cone Nose Tip

The PSE and HLNSE methods were used in Ref. [32] to study the disturbances induced by discrete roughness elements located on the nose tip of a blunt, 7-degree half-angle cone with a nose radius of 15.24 mm at freestream conditions selected to match those of the experiments presented in Ref. [15], i.e., $M_\infty = 5.9$, $T_\infty = 76.74$ K, $p_0 = 1526.23$ psi, which yield a $Re_\infty = 75.8$ m^{-1} by using the Sutherland's viscosity law. An isothermal wall temperature condition was used with $T_w = 300$ K. The axisymmetric boundary-layer flow is perturbed via an array of axially localized roughness elements centered at $\theta = 45°$ from the apex of the spherical tip, which is near the sonic line. The azimuthal wavenumber of the roughness elements

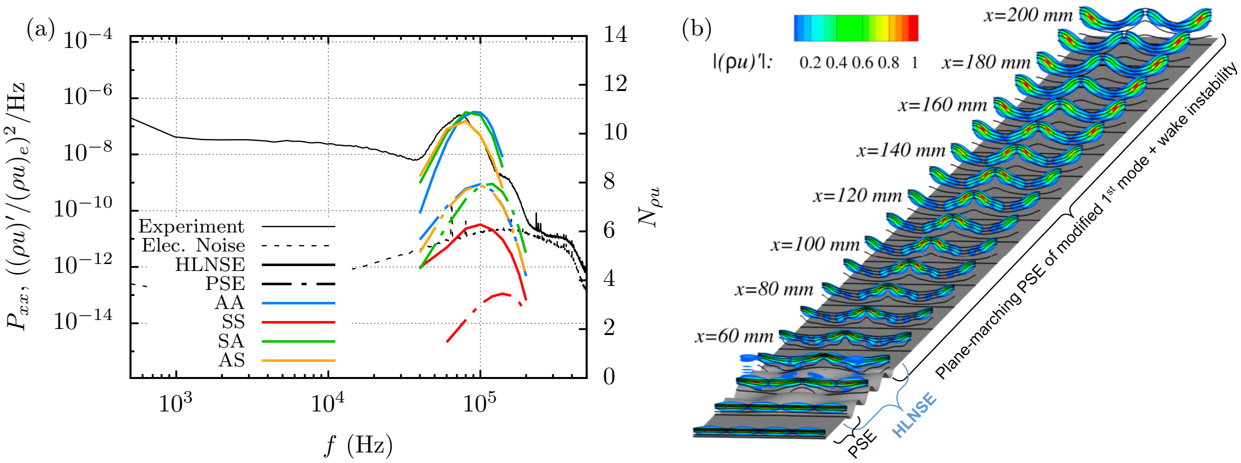

Figure 1: (a) Comparison of power spectra to most-amplified disturbances at $x = 153.8$ mm distance from the leading edge. The HLNSE results refer to the disturbance evolution calculated with a combination of plane-marching PSE and HLNSE, while the PSE results refer to the plane-marching PSE analysis of the roughness wake disturbances. (b) Disturbance streamwise mass flux contours and basic state isolines of AA disturbance with 80 kHz over the flat plate with a roughness patch. Adapted from Ref. [20].

equal to $m = 420$ was selected to match the optimal disturbance azimuthal wavenumber that leads to maximum transient growth [15]. The present results correspond to prismatic roughness elements with 20 μm height and width and length equal to 50% of the corresponding azimuthal wavelength. Similar to the previously discussed case of a flat plate with a roughness patch, the axisymmetric boundary-layer flow over a smooth cone was computed by using the second-order finite-volume Navier-Stokes solver implementation in VULCAN-CFD, and the three-dimensional, azimuthally-periodic, laminar boundary-layer flow with the roughness elements was computed with a seventh-order WENO-based DNS solver. Additional computational details are given in Ref. [32].

The instability characteristics of the perturbed, boundary-layer flow were examined by inflow-resolvent based on the HLNSE to capture the emergence and development of the disturbances in the immediate vicinity of the element and with plane-marching PSE to monitor the evolution of the streak instabilities that become amplified along the wake of the roughness elements [32]. Again, the disturbances are identified by their lateral boundary conditions, either symmetric (S) or antisymmetric (A), yielding four families of modes, AA, SS, SA, and AA. For the present strongly favorable-pressure-gradient boundary-layer flow over the nose tip of the blunt cone, and similar to previous studies with reentry capsules [39], the wake instabilities were found to reach their peak amplification within a few degrees downstream of the roughness element. For this particular case, the plane-marching PSE predicted the symmetric disturbances (SS and AS) to reach very similar maximum N-factor values of $N = 5.7$ at $\theta = 47.7°$, while the antisymmetric modes reached lower maximum amplification ratio of $N = 4.3$ at 49.4°. However, the maximum growth rate for the most amplified disturbances were found at the initial location for the PSE integration that coincided with the reattachment location behind the roughness element. To capture the evolution of the linear disturbances over the entire flow field, the inflow-resolvent analysis based on the three-dimensional HLNSE was used with a grid of $n_x = 701$, $n_y = 61$, and $n_z = 41$ points, which yield a linear system of 8.8M DOF. Due to the absence of unstable disturbances upstream of the roughness element, the optimal inflow disturbance was selected just upstream of the roughness elements at $\theta_0 = 44.36°$. Based on the PSE results, the downstream boundary of the optimization interval was selected at $\theta_1 = 47.4°$ to allow for the development of the streak instability modes. The N-factor spectra at $\theta = 48°$ calculated with the inflow-resolvent HLNSE and PSE methods are compared in Fig. 2(a). The shifts in N-factor values and the frequency bands for the symmetric and antisymmetric modes between the PSE and HLNSE predictions are rather significant and underscore the importance of accounting for the disturbance amplification within the region of separated flow for the present favorable-pressure-gradient configuration.

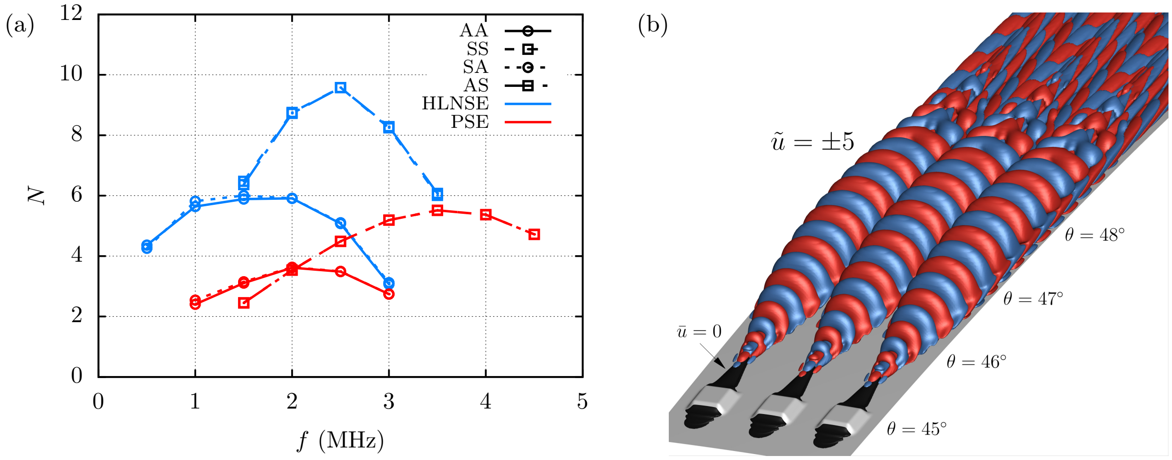

Figure 2: (a) Comparison of N-factor spectra of fundamental and subharmonic, symmetric and antisymmetric disturbances at $\theta = 48°$ from the axis. The HLNSE label refers to inflow-resolvent HLNSE results and the PSE label refers to the plane-marching PSE analysis of the roughness wake disturbances. Adapted from Ref. [32].

4 Conclusion and Future Work

The direct solution of the three-dimensional harmonic linearized Navier-Stokes equations (HLNSE) for transition prediction in flows with strongly nonparallel regions is performed. By using a fourth-order centered finite-difference standard scheme, the linear operator can be ordered as a block pentadiagonal (BPD) system of equations with complex arithmetic. The dual Schur complement method is used to split the problem into subdomains that are assigned to different MPI processors. Additionally, the Thomas algorithm is used to perform the factorization of the subdomains and exploit the OpenMP multithreaded sparse and dense matrix-vector and matrix-matrix operations with the crossplane blocks as implemented in algebra packages. Furthermore, the algorithm is explained for the multiple solutions of the direct and adjoint systems with a single factorization of the HLNSE operator for the solution of the global eigenvalue problem based on the Arnoldi method, or the resolvent analysis based on the iterative direct and adjoint solutions.

Two applications of the 3D HLNSE were shown for high-speed boundary layer configurations with rough surfaces. First, we presented a summary of the results shown in Ref. [20] on the evolution of Mack's first mode disturbances over a flat plate with a sinusoidal roughness patch at Mach 3.5 wind tunnel conditions. A remarkable agreement with the experimental measurements was found when the disturbance amplification upstream of, above, and downstream of the roughness patch was calculated with a combination of the parabolized stability equations (PSE) and the HLNSE methods. Second, the differences in disturbance amplification characteristics from PSE and inflow-resolvent HLNSE results are presented for a distributed roughness array located at the nose tip of a blunt cone at Mach 6 wind tunnel conditions from Ref. [32]. The PSE were used to calculate the linear amplification of roughness wake instabilities downstream of the reattachment location, but the inclusion of the near roughness vicinity and separation regions in the inflow-resolvent analysis based on the HLNSE led to a significantly higher amplification and a shift in the frequency bands.

Iterative linear solver methods will be evaluated in the future to overcome the restrictions of dense algebra required in the current implementation based on a direct solution.

Acknowledgments

This material is based upon research supported by the NASA Hypersonic Technology Project (HTP) under the Aeronautics Research Mission Directorate. Resources supporting this work were provided by the the NASA High-End Computing (HEC) Program through the NASA Advanced Supercomputing (NAS) Division at Ames Research Center and the NASA K-Midrange Cluster at Langley Research Center.

References

[1] P. Klebanoff and K. Tidstrom. Mechanism by which a two-dimensional roughness element induces boundary layer transition. *Physics of Fluids*, 15(7):1173–1188, 1972.

[2] Y. Wang and M. Gaster. Effect of surface steps on boundary layer transition. *Experiments in Fluids*, 39(4):679–686, 2005.

[3] M.E. Goldstein. Scattering of acoustic waves into Tollmien-Schlichting waves by small streamwise variations. *Journal of Fluid Mechanics*, 154:509–529, 1985.

[4] M. Asai, M. Minagawa, and M. Nishioka. The instability and breakdown of a near-wall low-speed streak. *Journal of Fluid Mechanics*, 455:289–317, 2002.

[5] D. Barkley, M.G.M. Gomez, and R.D. Henderson. Three-dimensional instability in flow over a backward-facing step. *Journal of Fluid Mechanics*, 473:167–190, 2002.

[6] J.-C. Loiseau, J.-C. Robinet, S. Cherubini, and E. Leriche. Investigation of the roughness-induced transition: global stability analyses and direct numerical simulations. *Journal of Fluid Mechanics*, 760:175–211, 2014.

[7] M. Choudhari and C. Streett. Theoretical prediction of boundary-layer receptivity. AIAA Paper 94-2223, 1994.

[8] J.D. Crouch, V.S. Kosorygin, and L.L. Ng. Modeling the effects of steps on boundary-layer transition. In Rama Govindarajan, editor, *IUTAM Symposium on Laminar-Turbulent Transition*, pages 37–44, Dordrecht, 2006. Springer Netherlands.

[9] J. Crouch, V. Kosorygin, and M. Sutanto. Modeling gap effects on transition dominated by Tollmien-Schlichting instability. AIAA Paper 2020-3075, 2020.

[10] C. A. Edelmann and U. Rist. Impact of forward-facing steps on laminar-turbulent transition in transonic flows. *AIAA Journal*, 53(9):2504–2511, 2015.

[11] Y. Guo, M. Malik, and C.L. Chang. A solution adaptive approach for computation of linear waves. AIAA Paper 97-2072, 1997.

[12] C. Streett. Direct harmonic linear Navier-Stokes methods for efficient simulation of wave packets. AIAA Paper 98-0784, 1998.

[13] M. Carpenter, M. Choudhari, F. Li, C. Streett, and C.-L. Chang. Excitation of crossflow instabilities in a swept wing boundary layer. AIAA Paper 2010-0378, 2010.

[14] C. Thomas, S.M. Mughal, H. Roland, R. Ashworth, and A. Martinez-Cava. Effect of small surface deformations on the stability of Tollmien-Schlichting disturbances. *AIAA Journal*, 56(6):2157–2165, 2018.

[15] P. Paredes, M. Choudhari, F. Li, J. Jewell, R. Kimmel, E. Marineau, and G. Grossir. Nosetip bluntness effects on transition at hypersonic speeds: experimental and numerical analysis. *Journal of Spacecraft Rockets*, 56(2), 2019.

[16] N. Hildebrand, M. Choudhari, and P. Paredes. Predicting boundary-layer transition over backward-facing steps via linear stability analysis. *AIAA Journal*, 58(9):3728–3734, 2020.

[17] A.P. Haas, O.M.F. Browne, H.F. Fasel, and C. Brehm. A time-spectral approximate jacobian based linearized compressible navier-stokes solver for high-speed boundary-layer receptivity and stability. *Journal of Computational Physics*, 405:108978, 2020.

[18] J.A. Franco, S. Hein, and E. Valero. On the influence of two-dimensional hump roughness on laminar-turbulent transition. *Physics of Fluids*, 32:034102, 2020.

[19] P.R. Amestoy, I.S. Duff, J. Koster, and J-Y. L'Excellent. A fully asynchronous multifrontal solver using distributed dynamic scheduling. *SIAM Journal on Matrix Analysis and Applications*, 23(1):15–41, 2001.

[20] A. Chou, P. Paredes, M. Kegerise, R. King, M. Choudhari, and F. Li. Transition induced by an egg-crate roughness on a flat plate in supersonic flow. *Journal of Fluid Mechanics*, (submitted), 2022.

[21] B.-T. Chu. On the energy transfer to small disturbances in fluid flow (Part I). *Acta Mechanica*, 1(3):215–234, 1956.

[22] L. M. Mack. Boundary layer stability theory. Technical Report Jet Propulsion Laboratory Report 900-277, California Institute of Technology, Pasadena, CA, 1969.

[23] A. Hanifi, P.J. Schmid, and D.S. Henningson. Transient growth in compressible boundary layer flow. *Physics of Fluids*, 8:826–837, 1996.

[24] M. Hermanns and J.A. Hernández. Stable high-order finite-difference methods based on non-uniform

grid point distributions. *International Journal for Numerical Methods in Fluids*, 56:233–255, 2008.

[25] L.H. Thomas. Elliptic probelms in linear difference equations over a network. Technical report, Columbia University, New York, 1949. Watson Sci. Comput. Lab. Rept.

[26] K. Benkert and R. Fischer. An efficient implementation of the thomas-algorithm for block penta-diagonal systems on vector computers. In Y. Shi, G.D. van Albada, J. Dongarra, and P.M.A. Sloot, editors, *Computational Science – ICCS 2007*, pages 144–151, Berlin, Heidelberg, 2007. Springer Berlin Heidelberg.

[27] V. Theofilis. Global linear instability. *Annu. Rev. Fluid Mech.*, 43:319–352, 2011.

[28] D. Sipp and O. Marquet. Characterization of noise amplifiers with global singular modes: the case of the leading-edge flat-plate boundary layer. *Theoretical and Computational Fluid Dynamics*, 27:617–635, 2013.

[29] X. Garnaud, L. Lesshafft, P. Schmid, and P. Huerre. The preferred mode of incompressible jets: Linear frequency response analysis. *Journal of Fluid Mechanics*, 716:189–202, 2013.

[30] D. Vanderstraten and R. Keunings. A parallel solver based on the dual Schur decomposition of general finite element matrices. *International Journal for Numerical Methods in Fluids*, 28:23–46, 1998.

[31] M. Choudhari, F. Li, P. Paredes, and L. Duan. Effect of 3d roughness patch on instability amplification in a supersonic boundary layer. AIAA Paper 2019-0877, 2019.

[32] P. Paredes, A. Scholten, F. Li, M. Choudhari, B. Price, and J. Jewell. Combined bluntness and roughness effects on cones at hypersonic speeds. AIAA 2022-0000, 2022.

[33] C.J. Roy and F.G. Blottner. Review and assessment of turbulence models for hypersonic flows. *Progress in Aerospace Sciences*, 42:469–530, 2006.

[34] D.K. Litton, J.R. Edwards, and J.A. White. Algorithmic enhancements to the VULCAN Navier-Stokes solver. AIAA Paper 2003-3979, 2003.

[35] R. Baurle, J. White, T. Drozda, and A. Norris. VULCAN-CFD theory manual: Ver. 7.1.0. NASA TM-2020-5000766, 2020.

[36] M. Wu and M.P. Martin. Direct numerical simulation of supersonic boundary layer over a compression ramp. *AIAA Journal*, 45(4):879–889, 2007.

[37] G.S. Jiang and C.W. Shu. Efficient implementation of weighted ENO schemes. *Journal of Computational Physics*, 126(1):202–228, 1996.

[38] J. Williamson. Low-storage Runge-Kutta schemes. *Journal of Computational Physics*, 35(1):48–56, 1980.

[39] A. Theiss, S. Hein, S.R.C. Ali, and R. Radespiel. Wake flow instability studies behind discrete roughness elements on a generic re-entry capsule. AIAA Paper 2016-4382, 2016.